J Mater Sci (2010) 45:2662–2669
DOI 10.1007/s10853-010-4245-6

The influence of high-temperature sintering on microstructure and mechanical properties of free-standing APS CeO_2–Y_2O_3–ZrO_2 coatings

M. Alfano · G. Di Girolamo · L. Pagnotta · D. Sun · J. Zekonyte · R. J. K. Wood

Received: 24 September 2009 / Accepted: 18 January 2010 / Published online: 4 February 2010

Abstract In this study, ceria–yttria co-stabilized zirconia (CYSZ) free-standing coatings, deposited by air plasma spraying (APS), were isothermally annealed at 1315 °C in order to explore the effect of sintering on the microstructure and the mechanical properties (i.e., hardness and Young's modulus). To this aim, coating microstructure, before and after heat treatment, was analyzed using scanning electron microscopy, and image analysis was carried out in order to estimate porosity fraction. Moreover, Vickers microindentation and depth-sensing nanoindentation tests were performed in order to study the evolution of hardness and Young's modulus as a function of annealing time. The results showed that thermal aging of CYSZ coatings leads to noticeable microstructural modifications. Indeed, the healing of finer pores, interlamellar, and intralamellar microcracks was observed. In particular, the porosity fraction decreased from ~10 to ~5% after 50 h at 1315 °C. However, the X-ray diffraction analyses revealed that high phase stability was achieved, as no phase decomposition occurred after thermal aging. In turn, both the hardness and Young's modulus increased, in particular, the increase in stiffness (with respect to "as produced" samples) was equal to ~25%, whereas the hardness increased to up to ~60%.

M. Alfano (✉) · L. Pagnotta
Department of Mechanical Engineering, University of Calabria, Ponte Pietro Bucci Cubo 44C, 87036 Rende, Italy
e-mail: alfano@unical.it

G. Di Girolamo
ENEA, Brindisi Research Center, S.S. 7 Appia, km 706, 72100 Brindisi, Italy

D. Sun · J. Zekonyte · R. J. K. Wood
National Centre for Advanced Tribology (nCATS), School of Engineering Sciences, University of Southampton, Southampton, UK

Present Address:
D. Sun
NIBEC, University of Ulster, Newtonabbey BT37 0QB, UK

Introduction

The technological demand for engines characterized by high efficiency and less fuel consumption is constantly driving the development of new and advanced materials. A meaningful example is represented by air plasma sprayed zirconia (ZrO_2) thermal barrier coatings (TBCs) which are currently adopted to protect core components of aircraft and/or land-based turbine engines from thermal fatigue, oxidation, and hot-corrosion [1]. In plasma spraying, the feedstock material is melted and accelerated by a plasma gas stream toward a substrate where it forms a protective coating characterized by a typical lamellar microstructure. It has been reported that the peculiar *splat*-like microstructure of as-sprayed deposits, characterized by networks of pores and microcracks, decreases coating stiffness, especially when compared to that of bulk ceramic material [2, 3].

However, during service yttria-stabilized zirconia (YSZ) TBCs can be exposed to high temperature (≈1300–1400 °C), as a consequence the closure of finer pores and microcracks, and then sintering of the porous microstructure, may occur [3–5]. The partial densification of coating microstructure leads to an increase in Young's modulus and, according to the level of stiffening, a corresponding decrease in strain tolerance can be observed [6–8]. In addition, upon slow cooling from service conditions to room temperature, a phase transition from tetragonal to monoclinic zirconia has been reported for typical YSZ systems, thus promoting cracking and lifetime reduction. On the other hand, the

Table 1 Plasma-sprayed parameters

	Current (A)	Turntable speed (rad/s)	Gun speed (mm/s)	Ar flow rate (slpm)	H_2 flow rate (slpm)	Standoff distance (mm)	Powder rate (g/min)
Top-coat	600	100	4	38	11	120	44
Bond-coat	600	50	4	55	11	120	50

slpm = standard liters per minute

addition of CeO_2[1] to YSZ provides ceria–yttria co-stabilized zirconia (CYSZ) which, in turn, can stabilize the high-temperature cubic phase and hinders the development of monoclinic zirconia. Ceria–yttria co-stabilized zirconia provides improved performances when severe operating conditions are expected [9–14]. In particular, recent studies focused on the properties of heat-treated CYSZ coatings, such as resistance to hot corrosion [11], chemical state and crystal structure [12], phase stability [13], thermal expansion coefficients, and specific heat capacity [14].

In this study, the microstructural and the mechanical properties of heat-treated APS–CYSZ (ZrO_2–25CeO_2–2.5Y_2O_3, CYSZ) coatings are investigated. To this aim, the properties of as-sprayed CYSZ coatings, which have been analyzed in an earlier study carried out by the authors [15], are herein employed as baseline to explore the evolution of coatings microstructure and mechanical properties. In particular, CYSZ samples are heat treated in air atmosphere at 1315 °C and the microstructural modifications, for increasing thermal aging time (2–50 h), are investigated by X-ray diffraction (XRD) and scanning electron microscopy (SEM). Image analysis is adopted to assess the variation of porosity level. Furthermore, both conventional and instrumented indentations tests are carried out in order to assess the influence of the heat treatment on the mechanical properties, i.e., hardness and Young's modulus. The results are in turn presented in statistical way using Weibull plots.

Materials and methods

Specimen preparation

CYSZ coatings were deposited on stainless steel substrates ($25 \times 25 \times 4$ mm^3) by atmospheric plasma spray equipped with a F4-MB plasma torch with a 6-mm diameter nozzle (Sulzer Metco, Wolhen, Switzerland). A commercial HOSP powder (Metco 205NS, Sulzer Metco, Westbury, NY, USA) was processed to manufacture 450-μm thick CYSZ coatings. Previously, the substrates were grit-blasted with abrasive alumina powder (Metcolite F, Sulzer Metco, NY, USA) and ultrasonically cleaned in ethanol. Moreover, a 150-μm thick metal bond coat was deposited by using a commercial CoNiCrAlY feedstock (Amdry 995C, Sulzer Metco). The substrates were placed on a rotating sample holder and then coated. Plasma spray parameters adopted in this study are summarized in Table 1.

It has been reported that the thermal stresses generated by the mismatch in thermal expansion coefficients between the coating and the substrate can hinder and retard sintering effects, for this reason comparative analyses are often carried out considering free-standing coatings, see [3, 7, 8] to list a few. Moreover, thermal stresses can also affect indentation responses and, as a consequence, hardness and Young's modulus determination [16–19]. Then, in this study, the sintering behavior of the coating has been observed on free-standing CYSZ samples. These last have been detached from the substrates using a 50/50 HCl–H_2O solution. Then, free-standing CYSZ coatings were cleaned by rinsing and infiltration of water, acetone, and ethanol, in sequence. The final samples were isothermally heat treated at 1315 °C in air atmosphere for 2, 10, and 50 h, respectively, using a heating rate of 6 °C/min and then slowly furnace cooled down to room temperature. It is well known that the overall effects of thermal aging on the microstructure are emphasized within the first 25–50 h of heat treatment [8].

Microstructural analyses

Phase analysis was performed on as-sprayed and annealed coatings using an X-ray powder diffractometer (PW 1880, Philips, Almelo, Netherlands), operating with Cu K_α ($\lambda = 0.154186$ nm) radiation produced at 40 kV and 40 mA. The 2θ scan was performed between 20° and 80° by a step size of 0.02°. Structural quantitative analysis was carried out by using the Rietveld technique and the free-domain MAUD software (Material Analysis Using Diffraction, version 2.074, Luca Lutterotti, University of Trento, Italy). The coatings were cut using a low-speed diamond saw, mounted in vacuum in polymer, ground with 20 and 10 μm diamond disks, and then polished using 6, 3, 1, and 0.25 μm diamond suspensions, respectively. The cross sections of as-sprayed and heat-treated coatings were observed by using an SEM (XL40, Philips, Eindhoven,

[1] Rare earth oxide with fluorite structure.

Netherlands). To prevent surface charging, a very thin gold film was deposited on each cross section. SEM images were acquired at different magnifications (×400, ×700, ×900, ×1200, ×3000) in order to cover large areas and to better observe all the typical microstructural defects of plasma-sprayed CYSZ coatings. The evolution of the microstructure which follows to thermal aging was studied by processing SEM images using a free-domain image analysis software (Image J, U.S. National Institutes of Health, Bethesda, MD, USA). Each image was auto-thresholded and transformed in binary image. Easy binary operations were employed to analyze the pore size and morphology in the coating microstructure.

Mechanical properties

Microhardness measurements were carried out on polished coating cross sections before and after heat treatment. To the purpose, a Vickers microindenter (Matsuzawa Seiki MHT-1) was employed. Measurements were performed at room temperature in air using a load of 300 gf and a dwell time of 10 s. The Vickers microhardness was calculated using the following equation [20]:

$$\mathrm{HV} = \frac{2P\sin\left(\frac{\theta}{2}\right)}{d^2} = 1.854 \cdot \frac{P}{d^2} \tag{1}$$

where P is the applied load, θ the angle between the opposite faces of the pyramidal indenter (136°), and d the mean diagonal of the indentation.[2] For each sample, the average was measured from the mean of at least 15 indentations, and the spacing between each of them was kept at least thrice the diagonal to avoid further stresses induced by mutual influence of consecutive indentations.

Moreover, hardness and Young's modulus of CYSZ coatings have been measured using depth-sensing nanoindentation (NI). Single-cycle NI tests were carried out on coating cross sections using a Nano-Test Platform 2 (Micro-Materials Ltd., Wrexham, UK) employing a Berkovich tip (radius <100 nm). For such test, selected samples were prepared using the same procedure as that adopted for SEM samples. An optical microscope allowed the user to select the indentation location on the cross section of the coating. The hardness and the reduced Young's modulus of the coating are determined from the analysis of the data corresponding to the unloading segment of the load–penetration (P–h) curves, following the procedures outlined by Oliver and Pharr [21, 22]. A typical P–h curve is reported in Fig. 1a. Figure 1b illustrates some characteristic parameters which come into play in the determination of the mechanical properties and which are introduced in what follows.

[2] The diagonals d_1 and d_2 of the indent left on sample surface at load removal were measured using an optical microscope.

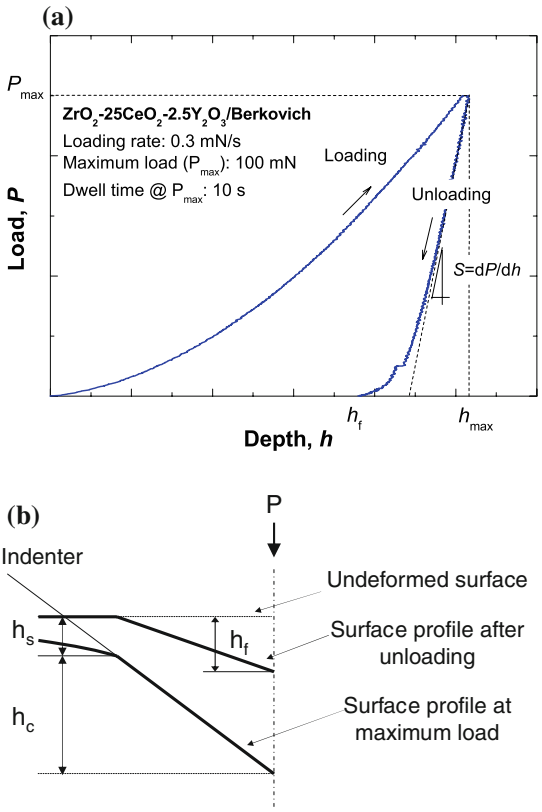

Fig. 1 **a** Typical load–penetration (P–h) curve obtained from an NI test. **b** Geometrical parameters related to key experimental quantities

The hardness (H) of the coating can be expressed as the ratio of the maximum applied load $P_{\max}$ to the projected indentation area A_c:

$$H = \frac{P_{\max}}{A_c}, \tag{2}$$

where $A_c = 24.5 \times h_c^2$ and h_c is the plastic (or contact) depth. Assuming that the contact area remains constant during initial unloading, the reduced Young's modulus E_r can be expressed using the equations given below:

$$E_r = \frac{1}{2\beta h_c}\sqrt{\frac{\pi}{24.5}}\left(\frac{\mathrm{d}P}{\mathrm{d}h}\right), \tag{3}$$

$$\frac{1}{E_r} = \frac{1-\nu^2}{E} + \frac{1-\nu_i^2}{E_i}, \tag{4}$$

$$h_c = h_{\max} - \varepsilon\frac{P_{\max}}{S}, \tag{5}$$

where $E_i = 1141$ GPa and $\nu_i = 0.07$ are Young's modulus and Poisson's ratio of the diamond indenter, E is the Young modulus of the coating, and β is a constant (equal to 1.034 for a Berkovich indenter) [20]. The contact depth h_c before unloading is estimated from the P–h curve, in particular, $S = \mathrm{d}P/\mathrm{d}h$ is the slope of the unloading curve, and ε is a

constant depending on the geometry of the indenter.[3] The holding time and the maximum load through the tests were set to 10 s and 100 mN, respectively, whereas the loading rate was set equal to 0.3 mN/s.

Results and discussion

Phase analysis

XRD spectra of as-sprayed and heat-treated CYSZ coatings are shown in Fig. 2a. The crystal structure of as-sprayed coating is composed of a mixture of metastable tetragonal t' and cubic c zirconia phases, as discussed in details in a previous related study [15]. The t' phase is formed from high-quenching rate of molten droplets upon their impact on the substrate, whereas the cubic phase derives from the starting feedstock. The addition of CeO_2 stabilizer to zirconia produces a distortion effect and an increase in lattice parameters for both tetragonal t' and cubic c phases. Indeed, the peak positions shift toward small angles in comparison with standard tetragonal and cubic zirconia phases. Due to peak overlapping between tetragonal t' and cubic c zirconia phases, peak deconvolution can be difficult. Therefore, the (400) reflections in the range between 71° and 75° have been considered for quantitative analysis. The Miller indices (hkl) denote the crystalline planes of zirconia. In Fig. 2b the (004) and (400) peaks for tetragonal t' zirconia and the (400) peak for cubic zirconia are detectable.[4] It should be noted that the (400) peaks for cubic and tetragonal zirconia are partially overlapped and their separation was automatically performed by the software. The volume fractions for cubic c and tetragonal t' zirconia phases, calculated by Rietveld analysis, are 16 and 84%, respectively ($c + t' = 100\%$). After thermal aging, a high phase stability is noticed, i.e., no phase decomposition occurs. Indeed, no monoclinic zirconia is observed in the range 27°–32° of the diffraction patterns. The volume fraction of cubic zirconia decreases with increasing annealing time, due to a diffusionless of cubic c to tetragonal t' zirconia, and it is equal to 8% after 50 h of thermal aging (t' phase = 92%). There is a small reduction of peak width at half maximum, which reveals a crystalline size growth during thermal aging.

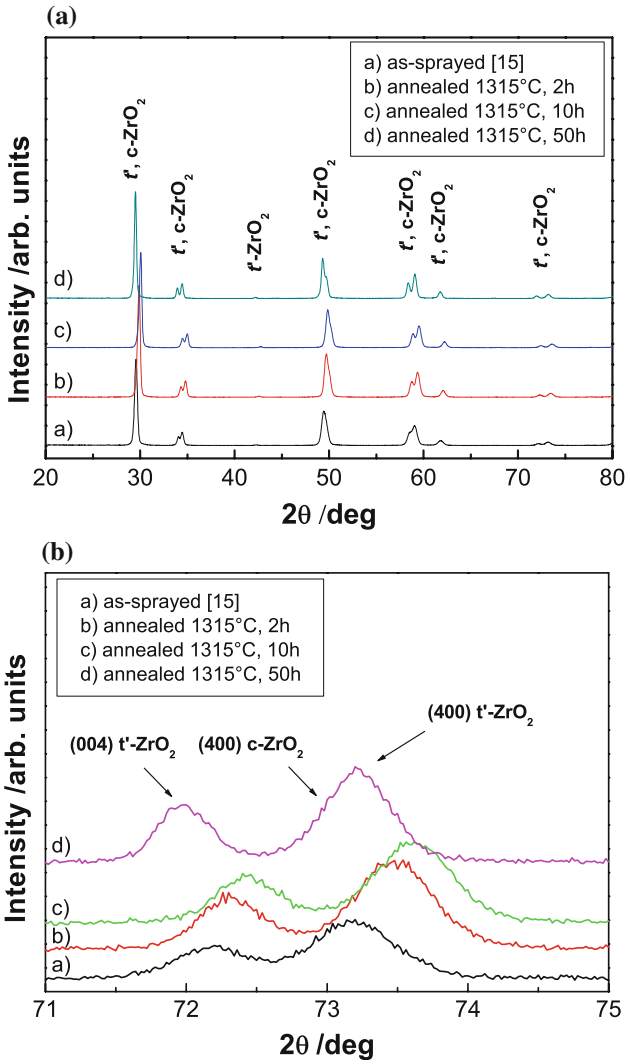

Fig. 2 **a** XRD patterns of as-sprayed and annealed CYSZ coatings. **b** High-angle region of XRD patterns

Microstructure

The as-sprayed CYSZ coating is typically characterized by a porous microstructure with lamellae parallel to the substrate and embedded in a network of globular pores, interlamellar and intralamellar microcracks [15]. After annealing, a partial sintering of the porous microstructure is observed. A comparison between the microstructures of annealed CYSZ coatings is reported in Fig. 3. It is apparent that the size and the distribution of both microcracks and globular pores are affected by thermal aging and a progressive closure of finer pores and microcracks can be observed with the progression of the thermal aging. In particular, Fig. 3d shows the microstructure of CYSZ coating annealed at 1315 °C for 50 h at higher magnification. The coating is not fully sintered after heat treatment, indeed pores and inter-splat microcracks

[3] $\varepsilon = 2(\pi - 2)/\pi$ for a Berkovich indenter.

[4] According to Joint Committee on Powder Diffraction Standards (JCPDS) No. 81-1544 and 49-1642 cards, available at International Centre for Diffraction Data (ICDD).

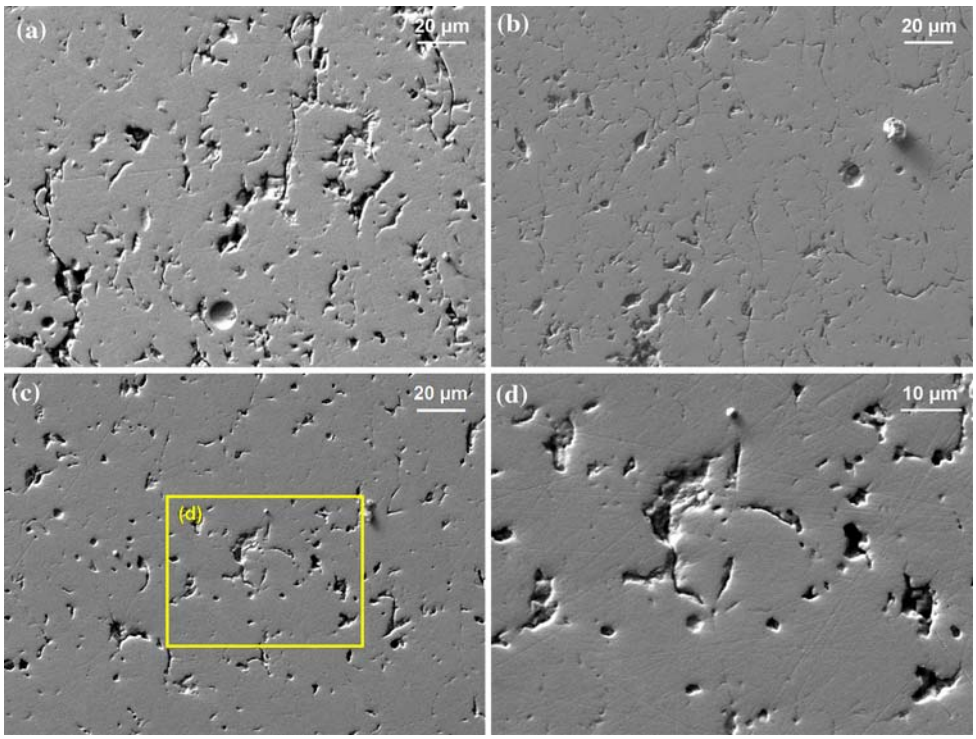

Fig. 3 Microstructure of annealed CYSZ coating after **a** 2 h, **b** 10 h, and **c**, **d** 50 h (Spraying direction from top to the bottom)

(approximately perpendicular to spraying direction) are partially retained, especially at the edge of the molten splats, where these defects show larger size. The intralamellar microcracks (approximately parallel to spraying direction) are still observable within the coating after the first hours of heat treatment but tend to disappear with increasing aging time. Moreover, Fig. 3c shows that the densification which follows the heat treatment affects only to a lesser extent the size and the distribution of the large globular pores.

It is worth noting that the nature of pores and interfaces plays an important role in the sintering behavior of plasma-sprayed coatings. Since the first hours of the heat treatment, the formation of sintering necks between the lamellae reduces the interlamellar porosity. In particular, after the heat treatment it is difficult to distinguish the original lamellar microstructure of the as-sprayed coatings [15]. This feature was also observed in a previous study carried out on air plasma-sprayed YSZ coatings [3].

Evolution of hardness and Young's modulus

The heat treatment affects the microstructure of CYSZ coating. In order to assess the corresponding influence on hardness, Vickers microindentation and depth-sensing NI were carried out. Hardness measurement is often a difficult task because of the heterogeneous microstructure of the coating, which is characterized by the presence of microcracks, pores, splat boundaries, and unmelted particles.

Accurate Vickers microhardness measurements rely on visual resolution of the residual indentation; however, the diagonal of the indentation, d, can be difficult to resolve, indeed the load should be low enough to avoid cracking, which otherwise occurs within the indentation site [23]. Then an accurate choice of the applied load must be done. Preliminary tests carried out by the authors indicated that a load of 300 gf avoids cracking and retains the resolution of the residual indentation.

As the heterogeneous microstructure of APS coating can lead to scattered data, a minimum of 20 indentations was performed on each coating cross section. The results have been in turn presented by means of Weibull statistics. In particular, the experimental data have been sorted in ascending order and the Weibull probability, defined as $\alpha = (i - 0.5)/N$, was assigned to each hardness and elastic modulus data. The Weibull plots corresponding to the microhardness data are reported in Fig. 4.

The mean value of the hardness is represented by the intersection of x-axis ($y = 0$) and the Weibull plot. On the other hand, information related to the experimental scatter are provided by the Weibull modulus, m, i.e., the slope of the line in the plot; in particular, a higher modulus represents low experimental scatter. Table 2 shows the values of the Weibull parameters pertaining to Vickers microhardness data obtained on as-produced and annealed CYSZ samples.

An increase in Vickers microhardness for increasing annealing time is observed, indeed the plots in Fig. 4 shift

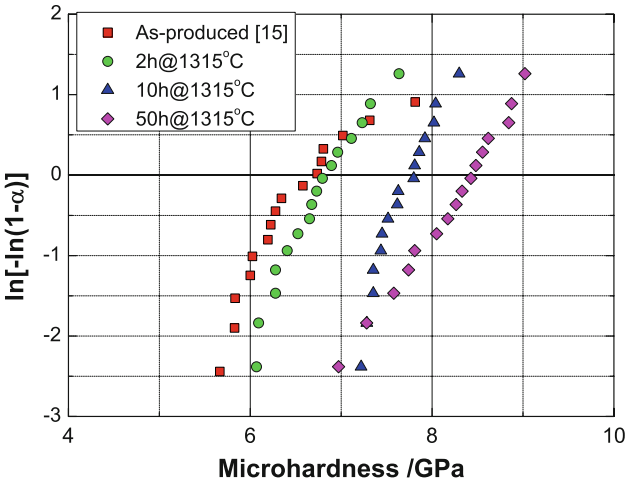

Fig. 4 Weibull plots of Vickers microhardness data

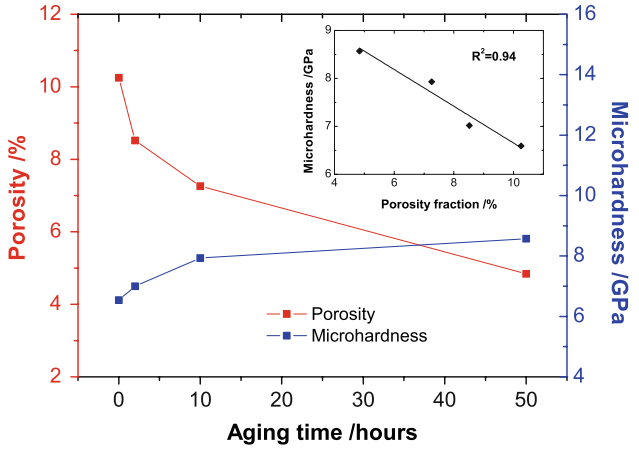

Fig. 5 Evolution of porosity level and microhardness as a function of the annealing time

Table 2 Microhardness data of as-produced and annealed CYSZ coatings

	HV[a] (GPa)	*m*
As-produced	6.5	19.1
Annealed, 2 h	7.0	12.4
Annealed, 10 h	7.9	24.6
Annealed, 50 h	8.6	14.9

[a] 300 gf/10 s

toward higher hardness for increasing aging time. This effect can be attributed to the partial sintering of the porous microstructure and is in agreement with the microstructural observations (Fig. 3). Similar behavior was also observed on heat-treated YSZ coatings [8]. In particular, the increase in microhardness is found to be 7% after 2 h, and it reaches 31% after 50 h of isothermal aging. Besides, there is not a clear trend in the Weibull modulus of microhardness data, as shown in Table 2. This feature could be attributed to the presence of globular porosity which has not fully recovered during the heat treatment; during the tests the indenter tip can impinge on these pores by leading to pronounced scatter in the experimental data. The initial porosity fraction of the coating is about ~10% [15]. However, as shown in Fig. 5, after 50 h at 1315 °C, the porosity decreases to ~5%. It is worth noting that the total porosity in the coating includes the contribution of globular porosity as well as the porosity derived from microcracks and splat boundaries.

The evolution of microhardness with annealing time is also reported in Fig. 5. Microhardness mean values progressively rise with annealing time. As expected, the graph shows a correlation between porosity and microhardness; in particular, form the inset in Fig. 5a linear relationship between microhardness and porosity fraction can be observed.

Similarly, consistent hardness measurements can be also obtained with the NI technique using low loads with no evidence of cracking. In this study, the NI tests were carried out using a maximum load of 100 mN. In addition, the reduced Young's modulus (E_r) of the coating can be also obtained by means of Eqs. 3–5.

A total number of 30 indentations were carried out for each sample obtained under different conditions. In particular, three set of ten indentations have been made in the through-thickness direction and the distance between each of them was equal to 40 μm; so that it is possible to avoid a mutual influence of consecutive indentations. Selected load–depth curves are reported in Fig. 6.

It can be observed that the maximum penetration depth (h_{max}) decreases with increasing annealing time, whereas the slope of the unloading curve increases. This behavior can be attributed to the progressive densification of the coating and results in increasing values of H and E_r, and it

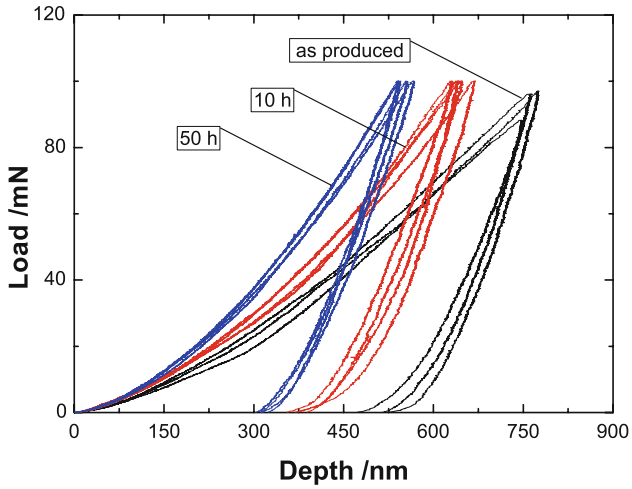

Fig. 6 Selected load–penetration (P–h) curves obtained during NI tests carried out on as-produced and heat-treated samples

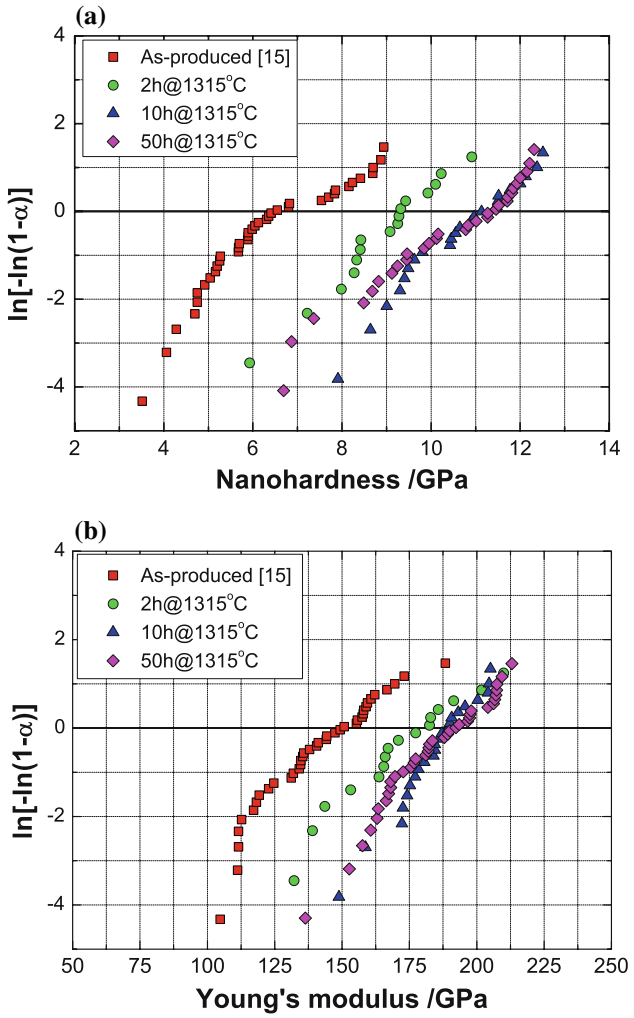

Fig. 7 Weibull plots of **a** hardness and **b** reduced Young's modulus determined by NI testing with a Berkovich indenter

is clearly shown by the Weibull plots in Fig. 7. In particular, a shift of the Weibull curves toward higher values of H and E_r can be observed for increasing aging time.

The corresponding Weibull parameters are reported in Table 3. The increase in nanohardness is rather sharp, indeed, Table 3 shows that H increases from 7.00 to 9.45 GPa (+35%) after 2 h and steps to 11 GPa (+60%) after 10 h. However, for longer aging time no further increase is observed.

These features are also illustrated in Fig. 8a, where H and E_r are reported as a function of the aging time. The inset in Fig. 8a also shows that a non-linear relation between the mechanical properties and the porosity seems to hold in this case.

Regarding the hardness, it is apparent that after 10 h of isothermal aging a plateau in the curve is reached. This point can be explained in terms of variation of the porosity fraction. Although large globular pores are not fully

Table 3 Hardness and reduced Young's modulus of annealed CYSZ coatings

	H^a (GPa)	m_H	E_r^a (GPa)	m_E
As-produced	7.0	5.2	152.7	6.9
Annealed, 2 h	9.4	8.2	181.8	9.3
Annealed, 10 h	11.2	10.0	190.7	15.0
Annealed, 50 h	11.0	7.2	192.8	11.8

[a] Loading rate: 0.3 mN/s; hold: 10 s

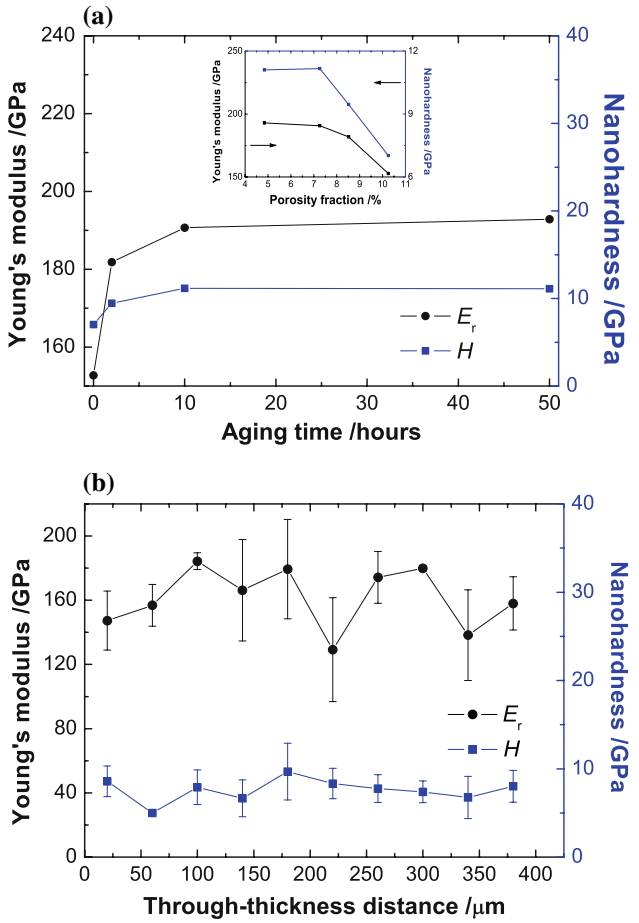

Fig. 8 **a** Evolution of E_r and H as a function of annealing time (the inset shows the variation of E_r and H with porosity). **b** Variation of E_r and H in the through-thickness direction (sample heat-treated for 50 h)

recovered after thermal aging,[5] the fine scale porosity (e.g., microcracks and poor inter-splat contact) largely responsible for low stiffness and low conductivity tends to be partially removed since the first hours of the heat treatment [3, 5, 7, 8].

[5] Globular porosity is not fully recovered after thermal aging because grain-growth across splats boundaries requires the splats to be in a fairly intimate contact [3].

As the size scale at which NIs are performed is comparable to the fine porosity observed in the coatings, it follows that NI data are mostly sensitive to these microstructural features; therefore, the hardness shows a plateau for greater aging times.

Moreover, it is worth noting that, comparing the results reported in Tables 2 and 3, a good agreement among nanohardness and microhardness values can be observed.

From Fig. 8a, it is also possible to appreciate a similar trend for the Young modulus (E_r); however, the increase in E_r after 10 h was lower and equal to 25%.

A similar behavior has been reported for APS YSZ coatings in [3, 7]. In particular, the initial increase in the mechanical properties (and then the high sintering rate) was therein addressed to the improved bonding and coherence across the splat boundaries. The subsequent step was characterized by a lower increase in stiffness and was addressed to the repair of microcracks. However, it is worth mentioning that in [3, 7] the stiffness of the coating was determined by means of static bending and a resonant-based method. Moreover, the deviation of mechanical properties in the through-thickness direction was not significant, as illustrated in Fig. 8b. So, the high-temperature sintering of CYSZ coating is uniform along coating thickness.

It is important to underline that E_r and H measured by NI could be affected by thermal residual stresses in the samples [16]. It has been demonstrated that this is an artifact caused by indenter-to-sample contact area variation due to the presence of thermal stresses and which is not taken into account for the analysis procedure (i.e. Eqs. 2–5) [17, 18]. However, these stresses mainly arise as a consequence of the thermal mismatch between the top-coat (ceramic) and the underlying layers (bond-coat and substrate). Unsupported (free-standing) ceramic top-coats are relatively unstressed and then the load–displacement curves obtained during NI (and in turn the mechanical properties) are unaffected by the standard data analysis procedure [19].

Conclusion

In this article, the sintering behavior of plasma-sprayed CYSZ coatings was investigated. The results showed that the aging of free-standing CYSZ coatings at high temperature (1315 °C) led to noticeable microstructural modifications. However, according XRD analyses no phase decomposition occurred after thermal aging. Indeed, no monoclinic zirconia phase was formed during cooling and only a diffusionless of cubic c to tetragonal t' zirconia phase could be noticed. The heat treatment produced the healing of finer pores, interlamellar, and intralamellar microcracks, thereby leading to a partial densification of the porous microstructure and, in turn, to a decrease in the porosity fraction ($\sim 10\% \rightarrow \sim 5\%$). As a consequence, the max penetration depth recorded during NI tests showed a decrease in increasing aging times, whereas the slope of the unloading curve increased. This behavior resulted in increasing values of the Young modulus. The increase in stiffness (with respect to as-produced samples) was equal to $\sim 25\%$. On the other hand, also micro- and nanohardness increased to values up to 60%. Follow-up work will consider a thermally cycled temperature history, as opposed to isothermal (the one analyzed herein). In addition, the effect of the presence of coating substrate (i.e., a condition more representative of industrial service) on sintering behavior will also be explored.

Acknowledgements The authors wish to thank C. Blasi (ENEA) for contribution in plasma spraying and P. Caliandro (OPTEL) for SEM observations.

References

1. Mencik J (1996) Mechanics of components with treated or coated surfaces. Kluwer Academic Publishers Group, Dordrecht
2. Kim HJ, Kweon YG (1999) Thin Solid Films 342(1–2):201
3. Thompson JA, Clyne TW (2001) Acta Mater 49:1565
4. Nusair Khan A, Lu J, Liao H (2003) Mater Sci Eng A 359:129
5. Tsipas SA, Golosnoy IO, Damani R, Clyne TW (2003) J Therm Spray Technol 13(3):370
6. Langjahr PA, Oberacker R, Hoffmann MJ (2001) J Am Ceram Soc 84(6):1301
7. Paul S, Cipitria A, Tsipas SA, Clyne TW (2009) Surf Coat Technol 203:1069
8. Basu D, Funke C, Steinbrech RW (1999) J Mater Res 14(12): 4643
9. Brandon JR, Taylor R (1991) Surf Coat Technol 46:91
10. Moon J, Choi H, Kim H, Lee C (2002) Surf Coat Technol 155:1
11. Park CSJ, Kim JH, Kim MC, Song HS, Park CG (2005) Surf Coat Technol 190:357
12. Ma B, Li Y, Su K (2009) Appl Surf Sci 255:7234
13. Tsipas SA (2010) J Eur Ceram Soc 30:61
14. Di Girolamo G, Blasi C, Schioppa M, Tapfer L (in press) Ceram Int. doi:10.1016/j.ceramint.2009.10.020
15. Alfano M, Di Girolamo G, Pagnotta L, Sun D (2009) Strain. doi: 10.1111/j.1475-1305.2009.00659.x
16. Tsui TY, Oliver WC, Pharr GM (1996) J Mater Res 11(3):752
17. Bolshakov A, Oliver WC, Pharr GM (1996) J Mater Res 11(3):760
18. Suresh S, Giannakopoulos AE (1998) Acta Mater 46(16):5755
19. Zhao X, Xiao P (2006) Surf Coat Technol 201:1124
20. Fischer-Cripps AC (2002) Nanoindentation. Springer-Verlag Mechanical Engineering Series. Springer-Verlag, New York
21. Oliver WC, Pharr GM (1992) J Mater Res 7(6):1564
22. Oliver WC, Pharr GM (2004) J Mater Res 19(1):3
23. Chowdhury S, de Barra E, Laugier MT (2005) Surf Coat Technol 193:200